THE ASTROPHYSICAL JOURNAL, 387:294–308, 1992 March 1

POSTEXPLOSION HYDRODYNAMICS OF SN 1987A

MARC HERANT
Harvard-Smithsonian Center for Astrophysics, 60 Garden Street, Cambridge, MA 02138
AND
WILLY BENZ
Steward Observatory, University of Arizona, Tucson, AZ 85721
Received 1991 July 11; accepted 1991 September 4

ABSTRACT

We present a comprehensive study of the postexplosion hydrodynamics of the ejecta of SN 1987A, encompassing the Rayleigh-Taylor instabilities at the shell interfaces and the dynamical effects of the energy input due to the radioactive decay of ^{56}Ni and ^{56}Co. In an attempt to explain the observed high-velocity wings of the iron line of SN 1987A, we investigate the dependence of the hydrodynamical behavior on progenitor structure, initial perturbations, explosion energy, and dimensionality of the numerical simulation. We show that none of these factors leads to the required high-velocity tail of iron, although we are able to reproduce the line core adequately. This failure points toward early instabilities which would premix the nickel outward during, or shortly after, the explosion itself, and therefore enable the nickel to participate in the subsequent round of Rayleigh-Taylor instabilities. By artificially premixing nickel in our initial model, we find that this early mixing has to affect the inner 1.5 $M_\odot$ of the ejecta to reproduce the high-velocity wings at a time of 90 days. We speculate that the high-entropy bubble associated with the delayed mechanism is responsible for this premixing by driving convective motions early in the explosion.

Subject headings: hydrodynamics — stars: individual (SN 1987A) — stars: interiors — supernovae: general

1. INTRODUCTION

The unexpected early detection in mid-August of 1987 X-rays from SN 1987A by the *Ginga* satellite and the Kvant-Mir space station (Dotani et al. 1987; Sunyaev et al. 1987) and later of γ-rays (Matz et al. 1988) has shown in a dramatic way that our understanding of supernova explosions is far from being complete. All models (Gehrels, MacCallum, & Leventhal 1987; Xu et al. 1988; McCray, Shull, & Sutherland 1988; Pinto & Woosley 1988a) indeed predicted that these high-energy photons would only be seen about one year after the explosion, when the expansion factor had become large enough for the optical depth to diminish sufficiently.

These observations understandably stirred up the interest of a large number of research groups. The general conclusion was that the observations could be explained only by assuming that a large amount of mixing is taking place during the early stages of the explosion (Pinto & Woosley 1988b; Fu & Arnett 1989; Woosley 1988; Arnett & Fu 1989; Shigeyama, Nomoto, & Hashimoto 1988). The mixing, if on very large scales, could also account for the apparent smoothness of the observed light curve, although uncertainties in the actual radiation transfer calculations are large enough that this should not be considered a definitive proof of hydrodynamical instabilities (Höflich 1988).

Earlier analytical work, mainly based on the stability of shocks propagating down simple power-law density distributions (Chevalier 1976), showed that for some density profiles, the matter behind the shock is indeed subject to instabilities. Later, Bandiera (1984) pointed out that mixing could occur as the result of these instabilities. More recently, Ebisuzaki, Shigeyama, & Nomoto (1989) and Benz & Thielemann (1990) simulated the explosion of a supernova progenitor with a one-dimensional code and used Rayleigh-Taylor (RT) and convective instability criteria to locate the unstable regions. They found that the most unstable zones lie at the two interfaces corresponding to the metals (mainly Si-Mg-O-C), helium, and hydrogen shells.

Two groups simulated the explosion in two-dimensional cylindrical geometry from a few minutes to a few hours after collapse. They showed that significant mixing does indeed occur (Arnett, Fryxell, & Müller 1989b; Hachisu et al. 1990; Fryxell, Arnett, & Müller 1991; Müller, Fryxell, & Arnett 1990; and a three-dimensional simulation in Müller, Fryxell, & Arnett 1991). Both sets of runs, performed with two different progenitors and two different Eulerian codes, show impressive finger/mushroom-like structures of metals and helium poking into the outer layers of the expanding hydrogen envelope by the time the shock breaks out of the star.

However, the maximum velocities for cobalt and iron derived from these sets of simulations are in disagreement with the observed line profiles for these elements (Spyromilio, Meikle, & Allen 1990; Haas et al. 1990; Tueller et al. 1990). These observations have shown that a small fraction of Co and Fe is traveling at velocities of order 3000 km s^{-1}, whereas the maximum cobalt velocities obtained in the simulations are of order 1300 km s^{-1}. Furthermore, these velocities were only reached if somewhat uncomfortably large perturbations (a few percent) were applied to the initial model. At that time, both groups expressed the hope that the discrepancy would be lifted by allowing for the additional release of nuclear energy due to the decay of nickel and subsequently cobalt into iron. Indeed, the energy available from radioactive decay is comparable to the bulk kinetic energy of the nickel (Woosley 1988).

Finally, Herant & Benz (1991, hereafter HB91) simulated the explosion with a two-dimensional cylindrical geometry smooth particle hydrodynamics (SPH) code from a time of 5 minutes to 3 months, taking into account the radioactive decay and using both progenitors used by the Arnett and Nomoto

groups mentioned above. They were able to demonstrate that the effect of the decay energy is mainly to make the nickel flow back in the direction of least resistance, toward the inner cavity left behind by the expanding envelope. The giant nickel bubble thus formed accounts for the core of the observed line profiles. However, only a 30% increase of the maximum nickel velocity is registered, which falls at least 1000 km s^{-1} short of the more than 3000 km s^{-1} required to interpret the wings observed in the spectra. Moreover, the simulations by HB91 can actually be considered as an upper limit to the boost in nickel velocity because of the "on-the-spot" radioactive energy deposition scheme used. Assuming an optically thick medium is justified at early time, but becomes at best a coarse approximation after 3 months.

This discrepancy, which we have dubbed "the nickel discrepancy" in the rest of this paper, is now well established. On one hand, independent observations in X-ray (Tueller et al. 1990) and infrared (Spyromilio et al. 1990; Haas et al. 1990) concur to show that at least a fraction of the nickel (at the time already decayed into cobalt and iron) has been accelerated in the explosion to a velocity above 3000 km s^{-1}. On the other hand, hydrodynamical simulations by three different groups (Arnett et al. 1989a; Hachisu et al. 1990; HB91) agree to give a maximum nickel velocity which, in the very best case, barely reaches 2000 km s^{-1}. Because these groups used three widely different hydrodynamical codes, and have checked their numerical convergence, one can in all likelihood rule out a purely numerical origin to the nickel discrepancy.

In their conclusion, HB91 isolated three possible origins for the nickel discrepancy: flaws in the structure of the supernova progenitor, two-dimensional effects, and instabilities linked to the explosion mechanism itself. These three points clearly have implications beyond the resolution of the nickel discrepancy in SN 1987A. They potentially affect our understanding of all supernova explosions and thus deserve to be investigated on their own merit. In this paper, we review each of these points. We describe the numerical methods which we have used for this work in § 2. In §§ 3 and 4, we treat the influence of the progenitor structure and the three-dimensional behavior. Having shown that neither of these effects solves the nickel discrepancy, we make the case in § 5 for earlier instabilities, linked to the explosion itself, which could premix the nickel outward. We identify the extent of the early premixing required to explain the high-velocity wings of the iron lines. All the results are summarized in § 6. In Appendix A we present a synoptic table giving quantitative velocity information about each of the simulations referenced in this paper. Finally, in Appendix B, we have included further details about our two-dimensional cylindrical SPH.

2. NUMERICAL METHOD

In our investigation of the postexplosion hydrodynamics of SN 1987A, we have used a combination of several different numerical methods to model the evolution of the flow: a one-dimensional spherical geometry Lagrangian code, a two-dimensional cylindrical geometry SPH code, and a three-dimensional Cartesian geometry SPH code. A general description of the one-dimensional Lagrangian code and the three-dimensional SPH code can be found in Benz (1990, 1991), while the basic characteristics of the two-dimensional SPH code are given in Appendix B of this paper. In this section we describe in some detail the numerical tools which pertain more specifically to the simulation of Type II supernova explosions.

Our procedure to model the hydrodynamics involves three steps. First, the early phases of the explosion are modeled using a one-dimensional, second-order accurate Lagrangian code with very fine zoning (2000 equal mass cells). The explosion itself is initiated in the following way. We start by capping the density profile of the progenitor using the value of the density at the mass cut. This results in the subtraction of approximately 90% of the mass of the neutron star from the progenitor. Then we deposit the appropriate amount of energy [(1–2) $\times 10^{51}$ ergs, 1–2 foes] below the mass cut (see § 3 for a discussion of initial energy deposition). The simulation is stopped shortly after the shock penetrates the hydrogen envelope ($t \sim 300$ s). Finally the matter corresponding to the remaining 10% of the neutron star mass is removed from the innermost zones of the model.

The second step consists in transforming the resulting one-dimensional structure into a two-dimensional cylindrical SPH representation. While such quantities as internal energy or velocity can be arbitrarily assigned to each particle, reproducing a given density structure within SPH can be a difficult task because density is not a local quantity but is determined by the contribution of neighboring particles weighted by their mass. For the mapping to the two-dimensional cylindrical SPH representation, we place particles at the intersection of concentric circles and spokes radiating from the center. The circles are separated by intervals given by the mass conservation equation:

$$\Delta s \propto \frac{m(r)}{s^2 \rho(s)} ,$$

where s is the distance to the center, $\rho(s)$ is the density at that distance, and $m(s)$ is the mass of particles at distance r from the z-axis. In order to increase resolution close to the center (i.e., where the nickel is), we have set $m(r) \propto r = s \cos \theta$, where θ is the angular separation from the equatorial plane. Since we only model a 60° wedge with periodic boundary conditions, we have $-30° \leq \theta \leq 30°$. For the three-dimensional simulation, we have used a similar technique with the particles positioned at the intersection of radial spokes and spheres.

The final step of the procedure is to evolve the explosion from 300 s to 90 days with our multidimensional SPH codes. We use a realistic equation of state with gas and radiation pressure ($P = aT^4/3 + R\rho T/\mu$). The mean molecular weight, μ, is determined locally from chemical composition. The energy release due to nickel and cobalt decays is included as a source term in the energy equation:

$$\left(\frac{du}{dt}\right)_{\text{decays}} = x_{\text{Ni}}(3.90 \times 10^{10} e^{-t/7.60 \times 10^5} + 7.21 \times 10^9 e^{-t/9.82 \times 10^6}) \text{ ergs g}^{-1} \text{ s}^{-1} ,$$

where t is the time since the explosion in seconds and x_{Ni} is the initial mass fraction of nickel. This "on-the-spot" energy deposition is accurate if the smoothing length (h) of each nickel particle remains larger than the optical depth (τ). We find for a typical run that at $t = 90$ days, $\langle \tau/h \rangle \sim 7$, which means that the local energy deposition approximation is indeed coarse, as mentioned in § 1. However, at $t = 20$ days, we have $\langle \tau/h \rangle \sim 1$, and by this time most of the energy has already been deposited. This shows that our calculations correspond to an upper limit

of the energy deposition which should be fairly close to the real situation. Analysis of the bolometric light curve of SN 1987A has given a mass of ejected nickel around 0.075 $M_\odot$ (Arnett et al. 1989a and references therein). In general, except for simulations with premixing (see § 5), we have therefore assumed that the inner 0.075 $M_\odot$ of material above the mass cut is 100% nickel. Because the numerical scheme is Lagrangian and because at $t \sim 300$ s all nucleosynthesis is over, tracking each chemical species is completely straightforward; every particle is tagged and carries information about its chemical composition.

The instabilities are seeded by random velocity perturbations introduced behind the shock when mapping the one-dimensional Lagrangian model to the multidimensional SPH representation. Particles from the SPH representation are binned in cells of an overlying grid. All particles in the same cell are given the same velocity perturbation, but the perturbation is random from cell to cell. We have found that the zoning of the grid does not influence the subsequent evolution much, provided that the grid scale is smaller than the typical length scale of the instabilities and the grid scale is larger than the numerical resolution of the run (i.e., that there are at least a few particles in each bin). Nearly all the runs presented here were performed with perturbations set on a grid with 10 radial bins and 3° per angular bin (typical wavelength of the instability $\sim 10°$–$15°$). Similarly, we have found that the amplitude of the perturbations does not influence our results much as long as it remains above 5% peak-to-peak (see Table 2, Appendix A).

This last point deserves elaboration: whether the $\pm 2.5\%$ lower bound has a numerical origin or a real physical significance is not yet well determined. Numerical discretization inherently introduces some amount of viscosity that suppresses the growth of instabilities of wavelengths shorter than a certain value. These shortest wavelengths are also the ones that grow fastest at the onset of the RT instability, and because of this, they play a critical role in the transition from the linear phase to the nonlinear phase. It may be that, since the low-pass filter of numerical discretization deprives the system of its preferred route to the nonlinear stage, compensation through the introduction of strong perturbations is required. To investigate this problem, one needs to study the influence of the amplitude of the perturbations versus resolution. This has recently been done by Hachisu (K. Nomoto 1991, private communication), who finds that as the resolution increases, the required perturbation amplitude does *not* tend to zero. This naturally leads one to seek a physical origin for large initial perturbations. Arnett et al. (1989b) have suggested thermonuclear flashes when the shock goes through the oxygen shell, but they do not give a full account of how this would take place. Another possible origin of the perturbations is the existence of a first round of instabilities during the very early stages of the explosion (see § 5).

Finally, we would like to address the issue of numerical convergence, which is crucial to all computer simulations. We have performed runs with our two-dimensional cylindrical SPH code using Nomoto's progenitor with particle number ranging from 3000 to 60,000. The resulting relevant velocity information for each chemical element considered is given in Table 2 (Appendix A). From these results, it is apparent that runs with 10,000–20,000 particles capture the salient features of the hydrodynamics. The ability of SPH to simulate the problem realistically with a comparatively low investment of computer time (3 days of CPU on a DEC 3100 with 20,000 particles to $t = 90$ days) has its root in the nature of the RT flow. In general, the RT instability is characterized by large, low-density bubbles of rising material and narrow, high-density spikes of falling matter. For grid codes the spatial resolution requirement is set by the width of the spikes, which may lead to an overresolution of the bubbles and a waste of computer time. Within the SPH approach, the higher density in the spikes automatically implies a higher resolution because of the increased concentration of particles, while the low-density bubbles retain a lower resolution, which is satisfactory provided that the bubbles are large.

3. VARYING THE PROGENITOR

The limitations of our understanding of the late stages of stellar evolution are perhaps best exemplified by the general surprise of the astronomical community at the fact that the progenitor of SN 1987A was a *blue* supergiant. It is therefore reasonable to ask whether the nickel discrepancy might have its origin in the use of a model that does not accurately reflect the internal structure of the real SN 1987A progenitor. For this reason, we have conducted numerical experiments to determine the extent of the mixing in four different progenitors provided to us by three different groups. Although there is no reason to believe that the spread in progenitor structures issued from various stellar evolution codes brackets the range of uncertainties associated with them (stellar evolution theorists talk to each other), this is the only way we can probe how such uncertainties might influence the mixing. In this section we also investigate the effects of variations in the explosion energy.

The most important characteristics of the progenitors which we have used are summarized in Table 1. Nomoto's progenitor refers to model 14E, which is described in Saio, Nomoto, & Kato (1988) and Shigeyama & Nomoto (1990). It has already been used in the multidimensional simulations of Hachisu et al. (1990) and HB91. Its particularity is that, although originating from a 20 $M_\odot$ star, Nomoto's progenitor has a mass of only 16.3 $M_\odot$, having lost the balance in a stellar wind. Arnett's progenitor is described in Arnett (1987) and was used in multidimensional simulations by Arnett et al. (1989b), Fryxell et al. (1991), and HB91. Unlike the other progenitors, it corresponds to a star at the end of its C/O burning stage, the underlying assumption being that the structure of the outer envelope which determines the growth of the RT instabilities does not change much afterward. The difference in the core structure compared with the other progenitors is evident in Figure 1. It should also be mentioned that this is the only progenitor for which we use an initial condition for our multidimensional simulations that we did explode ourselves. The initial condition we use ($t = 300$ s) is the same as the one used by Arnett et al. (1989b), which they obtained by evolving the initial explosion with a one-dimensional parabolic piecewise method

TABLE 1

PROGENITOR INFORMATION

Progenitor	M_{ejec}	M_{CO}	M_{He}	M_H
Woosley	16.5	0.7	3.8	12.0
Weaver	20.5	1.5	5.0	14.0
Arnett	14.5	1.5	2.8	10.2
Nomoto	14.5	2.2	2.1	10.2

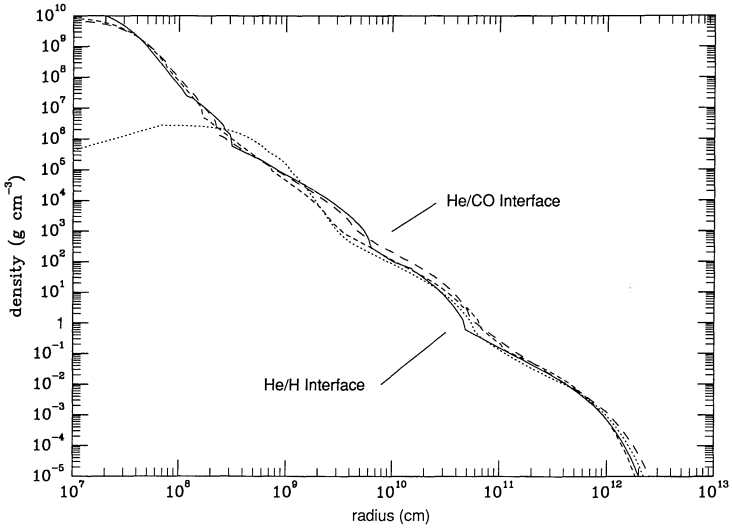

FIG. 1.—Density profile vs. radius for the four progenitors. *Solid line:* Nomoto's progenitor; *dotted line:* Arnett's progenitor; *short-dashed line:* Woosley's progenitor; *long-dashed line:* Weaver's progenitor.

(PPM) code. As a check, we were able to reproduce almost exactly their one-dimensional ($t = 300$ s) solution with our own second-order Lagrangian one-dimensional code. We should also point out that in their latest work Arnett et al. are apparently using a new progenitor, which should not be confused with the old one which we have been using. Finally, Woosley's progenitor (18 $M_\odot$) is described in Woosley, Pinto, & Weaver (1988), and Weaver's progenitor (22 $M_\odot$) will be described in Weaver & Woosley (1991).

It is difficult to predict, when given the one-dimensional profile of a progenitor, the kind of mushroom structure which will arise in a multidimensional simulation. This is because the final amount of mixing depends on many factors, ranging from the interaction of instabilities at the He/H and metals/He interfaces to the sharpness of the entropy jumps across these interfaces. In general, it appears that stronger discontinuities in entropy lead to more instability. The four progenitors have in common that the H/He interface gives rise to an instability of similar wavelength and amplitude, while, on the other hand, significant differences are apparent in the metals/He interface instability (Figs. 2 and 3). Both Woosley's and Weaver's progenitor models give rise to low-amplitude, small-wavelength instabilities at the metals/He interface. Arnett's progenitor gives rise to a fully grown crop of mushrooms at that interface, which, however, remains spatially separated from the He/H fingers. Finally, in the case of Nomoto's progenitor, metals/He instabilities grow strongly and merge with the He/H instabilities. From the point of view of the nickel discrepancy, it is Nomoto's progenitor which is most efficient at mixing material from the inner zones to the farthest radius out and the fastest velocities. Even then, it falls more than 1000 km s^{-1} short of what is required by the observations.

The differences in growth at the metals/He interface can be interpreted by examining the behavior of the density of each progenitor at this interface. The shock accelerates whenever the density distribution is steeper than r^{-3} (e.g., see Ryu & Vishniac 1991). When this occurs, the shock leaves behind a density which decreases outward. If the shock is later slowed because it encounters a shallower density gradient farther down the envelope (in the hydrogen layer, for instance), it generates a pressure wave (gradient) which opposes the previously generated density profile and thus leads to RT instabilities. The more the shock accelerates at the chemical interfaces because of a sudden drop in density, the steeper the postshock density gradient in that area, and thus the stronger the instability when the shock begins to slow down again. Clearly Arnett's and Nomoto's progenitors have a steeper density profile at the metals/He interface (Fig. 1), which may explain why they show stronger growth of the RT instabilities at this location.

Many techniques (none of them very realistic) have been used to generate explosions artificially in supernova progenitors for one-dimensional simulations (e.g., Aufderheide, Baron, & Thielemann 1991). Those include thermal bombs, pistons, and hybrid combinations of both with kinetic and thermal energy deposition. While the precise method used seems to influence early phenomena such as explosive nucleosynthesis, we have been able to verify that all these techniques yield similar profiles at $t = 300$ s. This is because, after going through a few solar masses of material, the shock has no memory of the initiation mechanism, and all that matters is the amount of energy deposited. Similarly, we have found that including or not including gravity in our simulations does not change the character of the structure of the ejecta at late times, but is rather akin to a change in the amount of energy deposited. Since the amount of gravitational binding energy is strongly dependent on the specific modeling of the inner zones of the supernova at the onset of the explosion, we have not used gravity in the simulations which we present in this paper. This allows for an accounting of the energy budget of the explosion which is much less model- and simulation-dependent. We have also found that changes in the explosion energy do not affect the amplitude or the wavelength of the instabilities, but rather modify all velocities by a factor approximately proportional to the square root of the explosion energy.

4. THREE-DIMENSIONAL VERSUS TWO-DIMENSIONAL EVOLUTION

In HB91, we pointed out that two-dimensional cylindrical geometry is only a crude approximation of a three-dimensional world. In particular, when extrapolated from two-dimensional cylindrical to three-dimensional Cartesian geometry, fingers

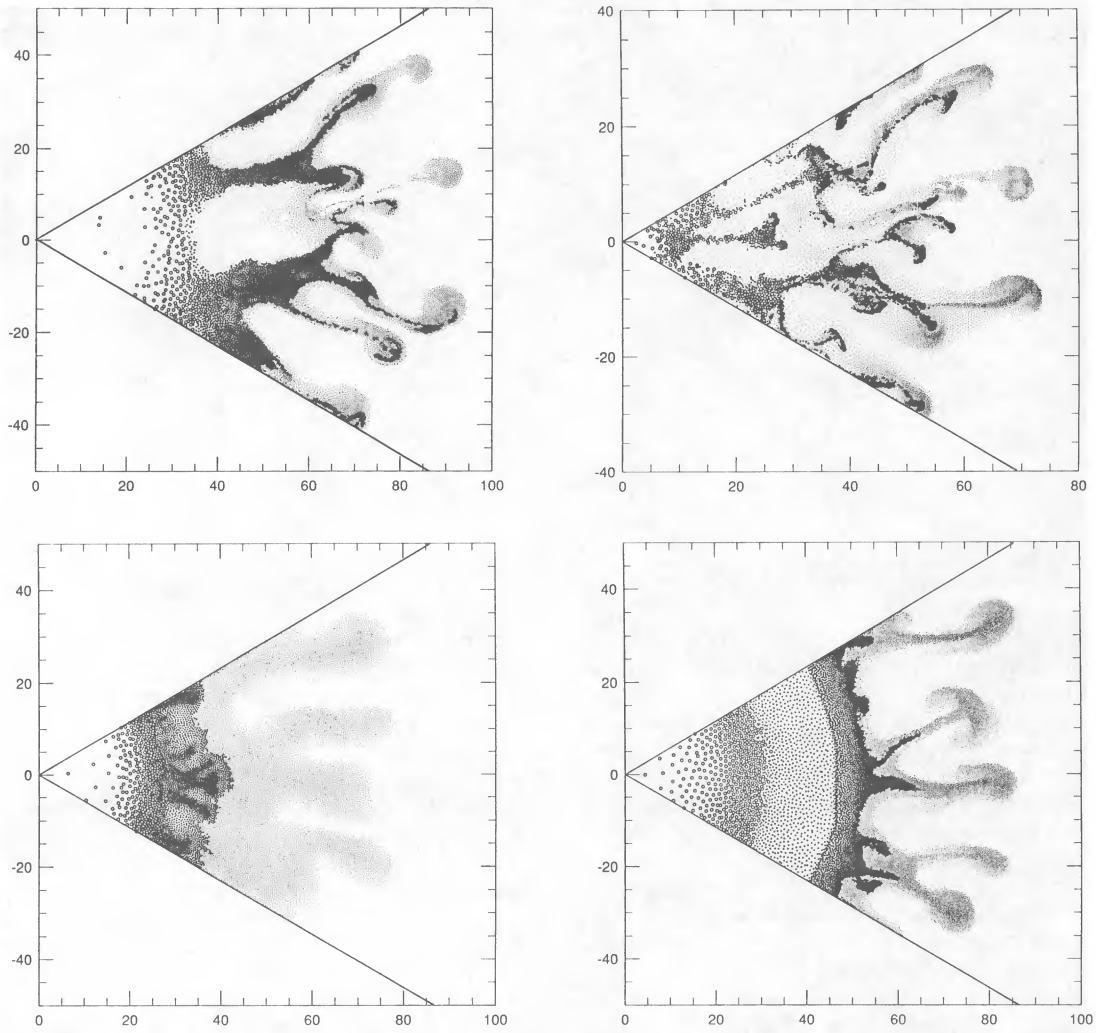

FIG. 2.—Four progenitors at $t = 400$ minutes. *Small dots:* helium particles; *large dots:* metal particles; *open circles:* nickel particles. Hydrogen particles are not shown because they are too numerous, but they fill the space between the fingers. *Top left:* Nomoto's progenitor; *top right:* Arnett's progenitor; *bottom left:* Woosley's progenitor; *bottom right:* Weaver's progenitor. Distance unit is $1 R_{\odot}$.

become curly sheets and there is no compelling reason to believe that these sheets accurately model three-dimensional fingers. Work by Layzer (1955) and more recently simulations by Tryggvason & Unverdi (1990) seem to indicate that during the nonlinear regime, the amplitude of the RT instability grows faster in three dimensions than in two dimensions. Therefore, it is essential to carry out three-dimensional simulations of the explosion to investigate possible differences between the two-dimensional and three-dimensional behavior of the system, as well as to determine the real three-dimensional morphology of the ejecta once the instabilities have set in. Unfortunately, a comprehensive set of simulations remains, for now, beyond our reach because of the tremendous computational effort which it would involve. It should suffice to say that we present here results from *one* simulation which used approximately five CPU *months* on a DEC 5000/200. More simulations are definitely in order to investigate the problem fully and verify that numerical convergence has been achieved, but these will not be feasible on our current machines. The use of supercomputers will eventually be required, although, as we discuss below, it is unlikely that higher resolution will result in velocities comparable to observations.

For our three-dimensional simulation we used the Nomoto progenitor evolved to $t = 300$ s using our Lagrangian one-dimensional code after a central energy deposition of 10^{51} ergs (see §§ 2 and 3). The computational domain is a square wedge with a 30° opening angle and with periodic boundary conditions. The number of particles used in the simulation is 100,000. As for our two-dimensional calculations, the mass resolution increases linearly toward the center; therefore the nickel particles are 20 times less massive than the outer hydrogen envelope particles. Random initial perturbations of amplitude $\pm 10\%$ in velocity were introduced behind the shock on an overlying grid of $10 \times 10 \times 10$ cells in angular and radial directions (see § 2).

Given the fact that we could run only one three-dimensional calculation, we have no indications whether or not the level of convergence and the sensitivity to the initial perturbations are similar to those found in two dimensions. Speculating that this is indeed the case, our three-dimensional simulation compares with a two-dimensional one using 8000 particles. We have compared results from such a two-dimensional simulation with our maximum-resolution two-dimensional case (60,000 particles) and found small differences in the velocity distribu-

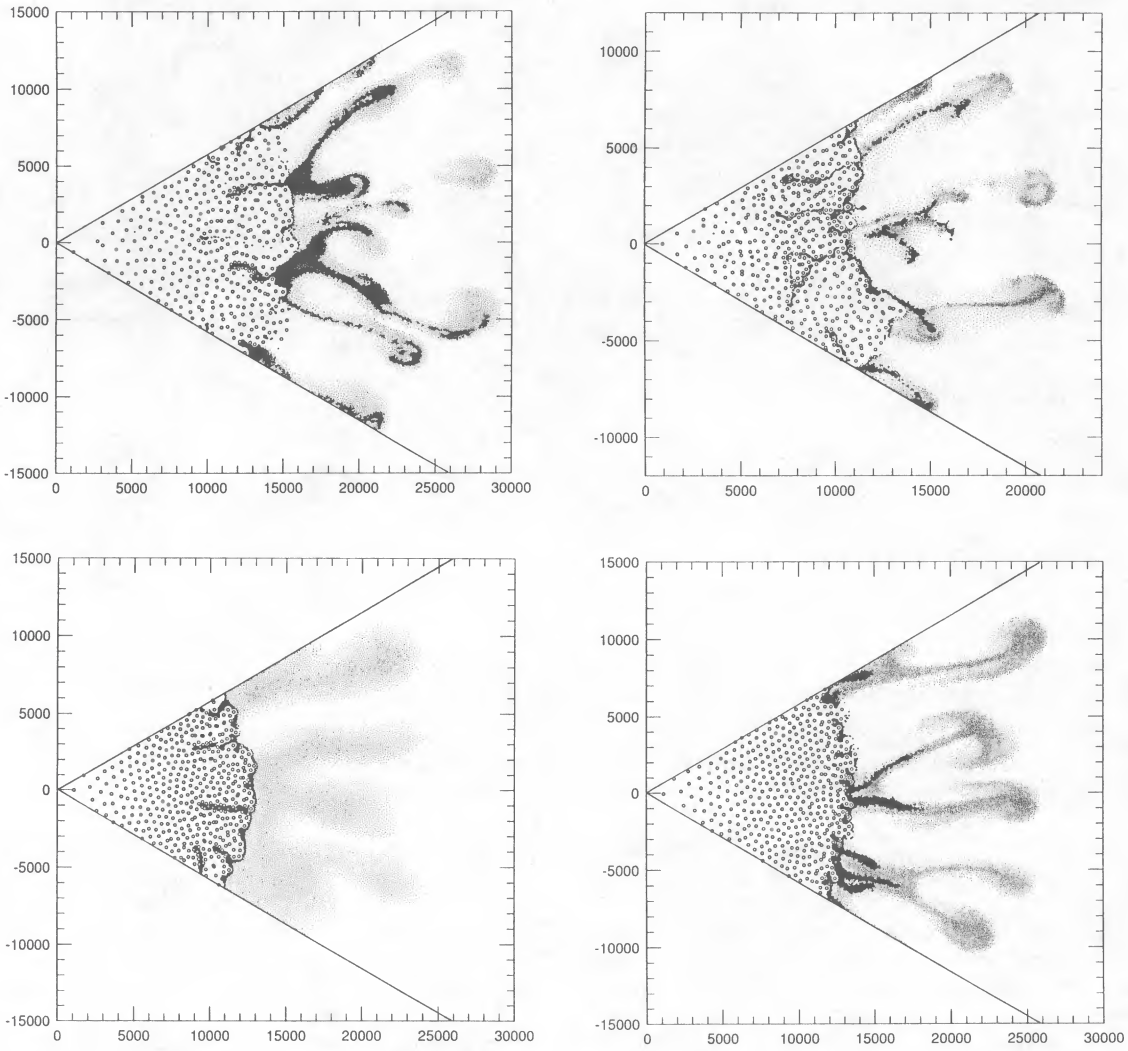

FIG. 3.—Same as Fig. 2, but for $t = 90$ days

tions and density profile. We can therefore claim that, if the numerical convergence proceeds in the same way in two dimensions and three dimensions, results from our three-dimensional run should be close enough to a converged solution to derive meaningful velocities.

4.1. *Velocities, Spectral Lines, and Light Curves*

Contrary to what we expected, and in agreement with Müller et al. (1990), the velocity distribution both before ($t = 400$ minutes) and after ($t = 50$ days) the radioactive decays does not change significantly from the two-dimensional case (Fig. 4). There seems to be a minimal, if any, increase in nickel velocity ($\sim 20\%$), but it is definitely not sufficient to cure the nickel discrepancy. The main difference between the two-dimensional and three-dimensional simulations is that hydrogen gets mixed inward deeper, and over a longer period of time: at $t = 1000$ minutes the minimum hydrogen velocity is 300 km s^{-1}. In other words, going from two to three dimensions changes the bubble amplitude but not the spike amplitude. Thus it appears that two-dimensional simulations do indeed give a correct estimate of the maximum velocities of each element in the ejecta, which is fortunate considering that almost all calculations performed so far were in two-dimensional geometry.

The lack of significant change in three dimensions was a surprise to us, for two reasons. First, the volume of the RT fingers in two-dimensional cylindrical geometry simulations is extrapolated by a 360° rotation around the z-axis. Therefore, even if the length of the fingers remains the same in two and three dimensions, there is no reason for the filling factor to remain unchanged. It is probable that the slight increase of nickel velocity which we observe in three dimensions has such an origin. Second, unlike other instabilities (e.g., Kelvin-Helmholtz), convective/RT instabilities do not have a global translational symmetry. Given that Müller et al. (1990) seem to reach the same conclusions using a completely different numerical method, we view these results as physical as opposed to numerical.

We have used our three-dimensional results to generate line profiles for the Ni/Co/Fe element (Fig. 5). In the optically thin limit (to be compared with IR observations; Fig. 10), we have, as in two dimensions, an adequate core of the line, but the high-velocity wings are absent. We have found that the viewing orientation does not affect the line shape very much. This is to

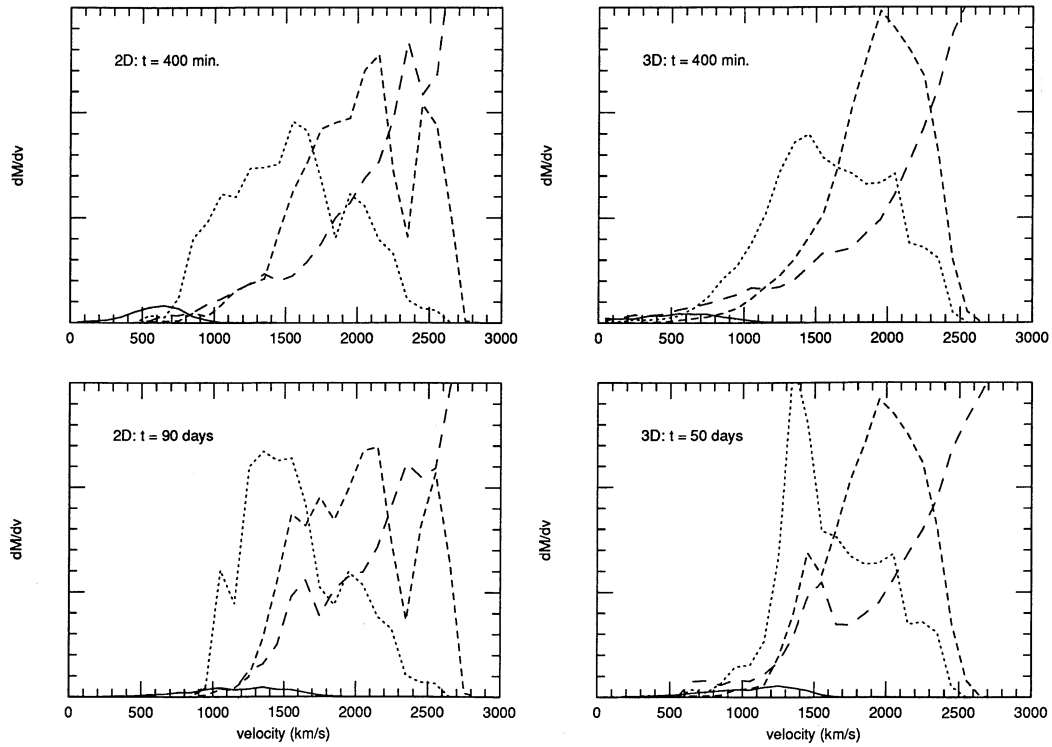

FIG. 4.—Velocity distribution of each chemical element for two-dimensional (*left*) and three-dimensional (*right*) simulations before and after nickel decay. The solid line corresponds to nickel, the dotted line to metals, the short-dashed line to helium, and the long-dashed line to hydrogen.

be expected, because the central nickel bubble is filled fairly uniformly. We have also computed γ-ray line profiles using ray-tracing on our three-dimensional model. Since our three-dimensional computational domain is a 30° × 30° wedge with periodic boundary conditions, collating six copies of the model along the sides results in a continuous half-wheel. This half-wheel can then be used for ray-tracing along its plane, because it presents a 30° triangle of "complete" star when projected onto the sky. As a check for spurious effects introduced by the periodicity of the replication process, we have ray-traced wheels constructed by collating our wedge in both the y- and x-directions (see Fig. 8). No significant changes were registered. Since we find that our final three-dimensional solution is very close to a homologous expansion, results for different epochs were obtained by homologously expanding the solution to the appropriate time. The ray-tracing was done using a realistic source function from cobalt radioactive decay and assuming an opacity originating from Klein-Nishina scattering of γ-rays by electrons. The Y_e's were determined from the local chemical composition. Figure 5 shows the 847 keV line at t = 300, 600,

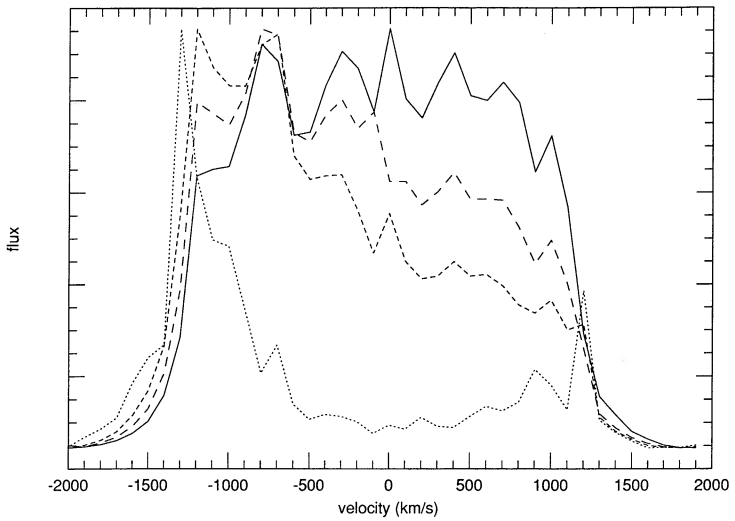

FIG. 5.—Line profiles at 847 keV. The solid line corresponds to optically thin ejecta, the dotted line to 300 days, the short-dashed line to 600 days, and the long-dashed line to 900 days. Each profile was normalized independently. Positive velocities correspond to a redshift.

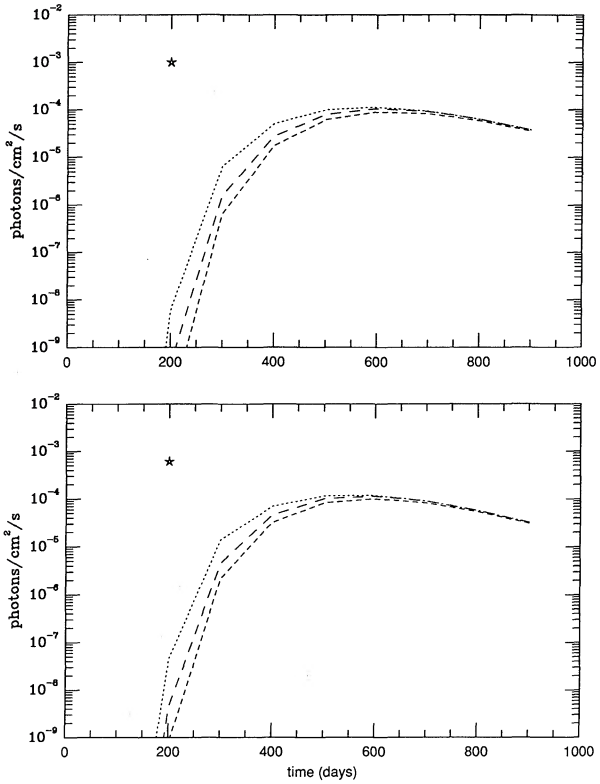

FIG. 6.—Gamma-ray light curves for three different viewing angles through the three-dimensional simulation. Stars represent *SMM* detections (Matz et al. 1988). *Top:* 847 keV line; *bottom:* 1238 keV line.

and 900 days. The line profile is blueshifted at the beginning but quickly becomes centered as the low-density, central nickel bubble becomes optically thin while the outer envelope is still optically thick.

We have also calculated γ-ray light curves for both the 1238 and the 847 keV lines with different viewing angles (Fig. 6). Our results give a peak luminosity at 500–600 days, much too late compared with observations (Matz et al. 1988). Viewing angle can shift the γ-ray light curve in time by up to approximately 40 days. We conclude from this that the early emergence of the γ-rays cannot be interpreted by the presence of "holes" in the ejecta. This is because the density contrast between fingers and bubbles is never more than a few, and tends to be compensated by the higher number of electrons per nucleon in the hydrogen-rich, low-density bubbles. It therefore appears that the early emergence of the γ-rays can only be explained by the presence of some nickel very far out in the envelope. These results once again confirm the existence of the nickel discrepancy, and reinforce the need for its resolution.

Finally, we would like to at least mention here the problem of the apparent redshift of the Ni/Co/Fe with respect to the rest frame of the supernovae. Both infrared (Spyromilio et al. 1990; Haas et al. 1990) and X-ray (Tueller et al. 1990) observations give line centroids which are redshifted by several hundred kilometers per second. While this redshift is at the limit of the spectral resolution of X-ray detectors, and although our limited knowledge of the formation mechanisms and opacities corresponding to the infrared iron lines make such line profiles difficult to interpret, the agreement of several types of observations makes a case for the reality of such a redshift. Unfortunately, we can only say that we are at a loss to explain such a break in the spherical symmetry. Our three-dimensional calculation indicates that the RT instabilities generate approximately 200 cells for the whole star, too many to potentially yield a significant redshift for a particular viewing angle.

4.2. *Three-dimensional Morphology*

Figures 7 and 8 show the complex structure which appears in the ejecta before ($t = 400$ minutes) and after ($t = 50$ days) the radioactive decays. A typical convective cell pattern is obvious in the top views of the wedge, showing bubbles of hydrogen separated by walls containing metals and helium. The angular size of the hydrogen cells is of order $\sim 15°$–$10°$, while the separating regions are about 5 times less wide. As should be expected, the dominant wavelength does not change from a two-dimensional to a three-dimensional simulation, since it is self-selected among competing modes during the linear phase of the instability, which is independent of dimensionality. As for the two-dimensional case, the main effect of the nickel and cobalt decays is to create a giant ^{56}Fe bubble in the center of the expanding envelope. Some amount of hydrogen, helium, and metals is trapped in the bubble and strongly compressed into small, high-density clumps.

Beyond SN 1987A, these conclusions about the three-dimensional morphology of the ejecta after instabilities and decays are over may have important implications for our understanding of one of the most famous supernova remnants (SNRs): the Crab Nebula. It has long been known that helium is overabundant in the Crab's filaments (Fesen & Kirshner 1982; MacAlpine et al. 1989; MacAlpine & Uomoto 1991), and this has led to speculations that the filaments were part of the ejecta rather than condensations of the interstellar medium. Clark et al. (1983) investigated in detail the three-dimensional structure of the Crab Nebula and concluded that the filaments extend between an inner shell and an outer shell (see their Fig. 9). Finally, de Gouveia Dal Pino & Opher (1989) showed that the filaments can be produced through a thermal synchrotron instability if the magnetic field is weak enough and if the ejecta was initially appreciably inhomogeneous. As a quantitative parameter of inhomogeneity, they defined

$$f_c = \frac{(A/V)_i}{(A/C)_s},$$

where $(A/V)_i$ is the area-to-volume ratio of the source (in our case, the He/H interface) and $(A/V)_s$ is the area-to-volume ratio of a sphere of equivalent radius (in our case, the He/H interface without mixing). De Gouveia Dal Pino & Opher (1989) required $f_c > 20$.

Our three-dimensional results have been obtained with a progenitor specifically tailored to match the characteristics of SN 1987A, which may have been very different from those of the Crab supernova. However, the similarities between instabilities from different progenitors (see § 2) lead us to think it appropriate to use our three-dimensional result at 90 days as a zeroth-order approximation to the early Crab SNR. We can then interpret the inner shell as a vestige of the boundary which marked the extent of the low-density nickel bubble. We have also used our three-dimensional result to compute the inhomogeneity parameter, and find $f_c \sim 30$–40, in line with what is required to seed the thermal instabilities in the Crab.

5. INSTABILITIES IN THE EARLY STAGES OF THE EXPLOSION

The apparent failure of all simulations published to date to reproduce the high-velocity tail of the nickel velocity distribu-

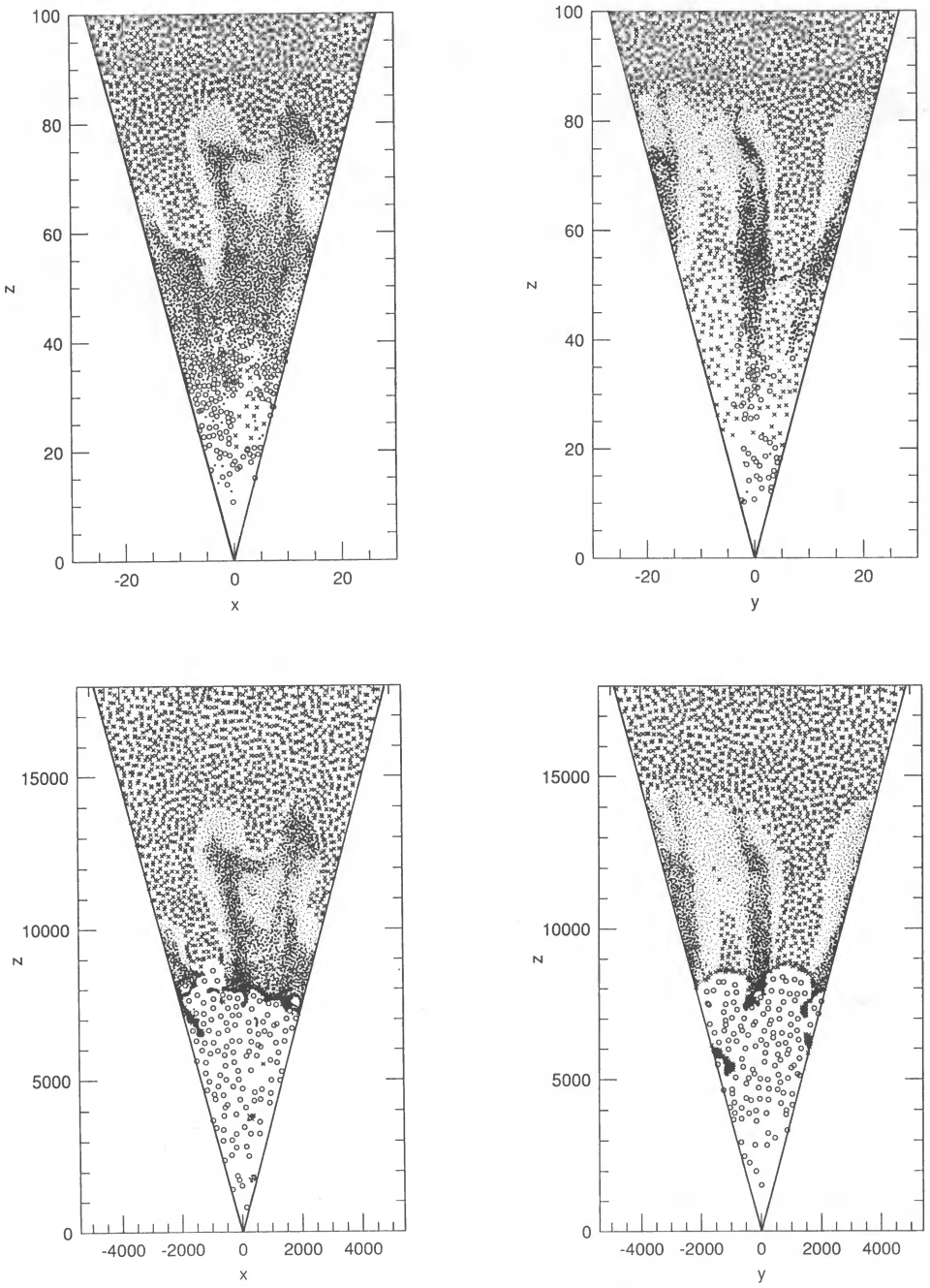

FIG. 7.—Plots of the particles in a slice (1° opening) for the three-dimensional simulation at $t = 400$ minutes (*top*) and at $t = 50$ days (*bottom*). Crosses are hydrogen particles, small dots are helium particles, large dots are metal particles, and open circles are nickel particles. Distance unit is 1 $R_\odot$.

tion strongly suggests that some crucial piece of physics is still missing in these models. We have shown above that the use of different progenitors, different initial perturbations, or three-dimensional models fails to significantly increase the maximum velocity reached by the nickel in the ejecta. Moreover, the close agreement between all simulations compared with the magnitude of the nickel discrepancy allows us to safely rule out a numerical origin (technique, resolution, geometry, etc.) of this problem. We can only conclude that an additional effect, not modeled so far, is providing an extra boost to at least a small fraction of the nickel. Since we believe that, by the time we start our multidimensional simulations, all the relevant physics is included, this additional mechanism can only operate sometime during the first 300 s. This naturally points toward the still elusive explosion mechanism. We argue here that using multidimensional hydrodynamics simulations coupled with velocity determinations of elements formed close to the neutron star (such as ^{56}Ni), we can probe the processes taking place in the deep interior of the supernova and obtain clues which should ultimately help us to understand the explosion mechanism itself.

From our simulations, it appears that if the 0.075 $M_\odot$ of nickel is located at the base of the ejecta at $t \sim 300$ s, it is impossible to accelerate even a small fraction to about 3000

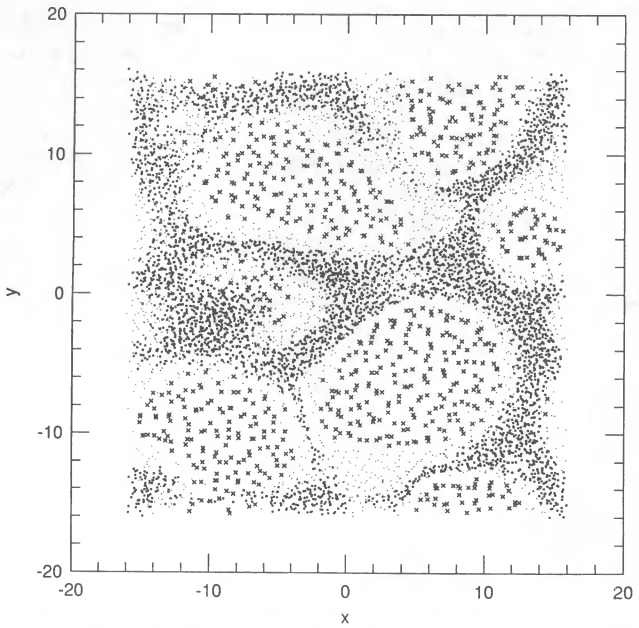

FIG. 8.—Particle plot for the three-dimensional simulation at $t = 400$ minutes for $55\ R_\odot < z < 60\ R_\odot$. Conventions are the same as for Fig. 7.

km s^{-1} during the subsequent instabilities. However, if during the explosion itself, or shortly thereafter, a first instability was present that already had mixed some nickel farther out in the ejecta, the later instabilities could carry this fraction toward still higher velocities. Interestingly, we note that the maximum velocity reached by the metals brackets 3000 km s^{-1}, depending on the initial explosion energy assumed in the simulations (Table 2).

5.1. *Very Early Instabilities and Mixing*

The detailed mechanism of the collapse and subsequent initiation of the explosion can be qualified at best to be poorly understood. Colgate (1991) has repeatedly emphasized the importance of the high-entropy bubble in order to insulate the neutron star from material falling back onto it. His argument is mainly that a rarefaction wave will inevitably appear behind the outgoing shock, and that since neutrino cooling at the relevant temperatures is extremely efficient, the only way to prevent a large amount of mass from accreting onto the neutron star in the minutes following the explosion is to shield it with a bubble of radiation. The existence of such a bubble is also predicted by the so-called delayed explosion mechanism (Mayle & Wilson 1991), in which the bubble is the driving force of the explosion.

The presence of huge entropy gradients in the delayed explosion mechanism clearly presents opportunities for very early mixing of the inner layers. Further, because neutrino heating from below (close to the proto–neutron star surface) takes place on a time scale which is long compared to the free-fall and sound-crossing time scales, it might sustain convection for an extended period. We are currently investigating this problem, and it will be discussed in depth in a forthcoming paper (Herant, Benz, & Colgate 1991).

Alternatively, Mönchmeyer & Müller (1989) and Mönchmeyer (1989) have recently simulated the collapse of rapidly rotating cores and shown that polar jets appear during the bounce. These jets are formed because the collapse proceeds faster along the axis parallel to the rotation axis, and thus the bounce is more efficient in that direction. It is possible that the jets might propel a significant amount of nickel to high velocities in the polar directions. However, current work (Baron & Cooperstein 1990) seems to show that prompt explosions will fail for a mass of the iron core corresponding to stars such as the most probable progenitors for SN 1987A. It is therefore likely that delayed neutrino heating will also play an important role in the explosion, even with a rapidly rotating core, and it is unclear how such heating will interact with the jets. Once again, more work is clearly needed in this area.

5.2. *Simulations with Premixed Nickel*

Early evidence for mixing in SN 1987A was provided by attempts to model the light curve using one-dimensional radiation transport codes. Such attempts showed that it is impossible to reproduce the observed light curve if chemical elements are kept segregated in their own shells. In order to explain the observations successfully, it was found that it is necessary to assume a certain amount of chemical mixing across shells (Pinto & Woosley 1988b). Since then, this mixing has been satisfactorily interpreted as the result of RT instabilities. We have adopted a similar approach for the problem of the nickel discrepancy. Since we know that the early stage of the explosion has the potential to give rise to hydrodynamical instabilities, it makes sense to try to determine qualitatively the amount of nickel premixing (at $t = 300$ s) which is needed to account for a high peak velocity for iron.

Because it is the model which gives the highest peak velocities (see § 3), we have chosen to use Nomoto's progenitor to explore the effects of various radial dependences of nickel premixing with two different explosion energies. Since we need the maximum velocity for nickel to be comparable to the top velocity attained by the metals, premixing through a significant portion of the CO shell is required. We have found that in order to mix nickel to the "mushroom caps" at $t = 400$ minutes, we need to premix nickel out to 75% (by mass) of the metals, which translates to premixing out to 1.5 $M_\odot$ above the mass cut. Notice that this is a large amount, but that for the other progenitors, the requirements would be even more drastic.

Figure 9 summarizes our results, while Figure 10 gives line profiles observed for iron at $t = 377$ days and $t = 407$ days. The line profiles of Figure 9 drawn as solid lines clearly illustrate the failure to reproduce observations in the absence of premixing. It is also clear that a quadratic or exponential radial dependence of the nickel premixing does not account for the distinctive wings of the observed line. On the other hand, uniform premixing gives a high-velocity tail with the appropriate amplitude compared with the central peak of the line. This behavior can be explained as follows. As was mentioned in § 1, the heating from radioactive decays tends to make the nickel flow inward, toward the central cavity left by the blast wave. This strongly suppresses the high-velocity wings of the iron line, *unless* a substantial amount of nickel is premixed far from the mass cut. Finally, an explosion energy of 2 foes (see § 3 for a discussion of explosion energies) gives a maximum velocity of 3000 km s^{-1}, which is what is required to lift the nickel discrepancy.

6. CONCLUSIONS

Observations of Co and Fe line profiles (Spyromilio et al. 1990; Haas et al. 1990; Tueller et al. 1990) show convincingly

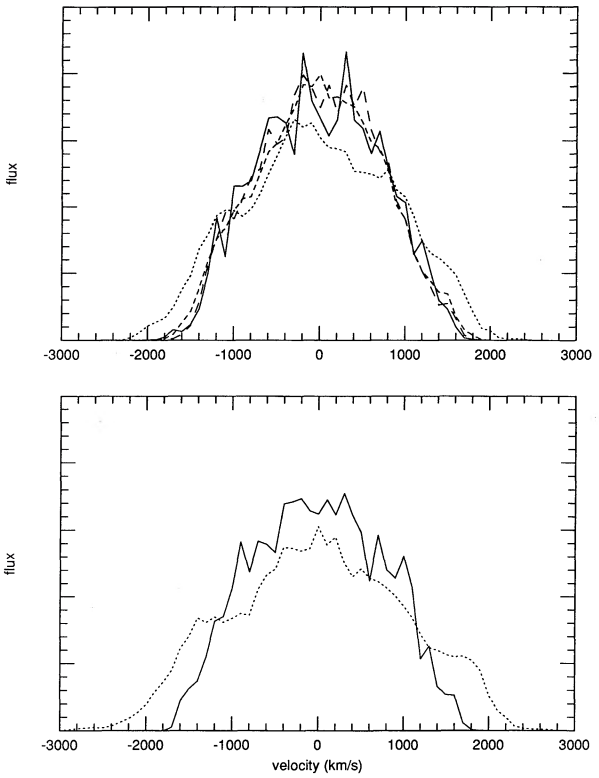

FIG. 9.—Nickel line profiles for optically thin ejecta at $t = 90$ days. The solid line corresponds to no premixing, the dotted line to uniform premixing, the short-dashed line to premixing with inverse-square dependence on radius, and the long-dashed line to premixing with inverse exponential dependence on radius. In each premixed model, nickel is initially mixed up to 1.5 $M_\odot$ above the mass cut. Positive velocities correspond to a redshift. *Top:* 1 foe; *bottom:* 2 foes.

that at least a small fraction of the original radioactive nickel must have a velocity as high as 3000 km s^{-1}. In this paper we show that these observations are impossible to explain within the framework of all numerical simulations presented here as well as published in the literature to date. We show that these measurements provide powerful tools to probe, in conjunction with multidimensional hydrodynamical simulations, the deepest layers inside the progenitor, and thus derive clues that should lead to a better understanding of the explosion mechanism.

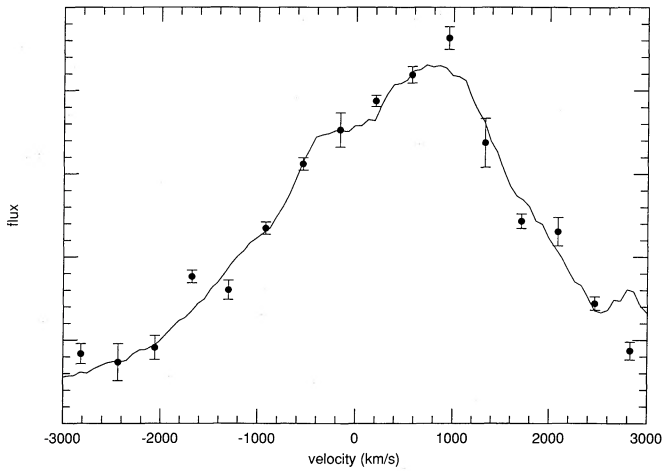

FIG. 10.—Observed infrared line profiles for Fe at 1.26 μm (*solid line*, $t = 377$ days: Spyromilio et al. 1990) and at 18 μm (*data points*, $t = 407$ days; Haas et al. 1990). Positive velocities correspond to a redshift.

We have investigated the sensitivity of the velocity distribution within the ejecta to the detailed internal structure of the progenitor by using four different progenitor models for SN 1987A. We have shown that the *maximum* velocity reached by ^{56}Ni or its decay products 90 days after the explosion, v_{max}(Ni), is significantly smaller than implied by observations. Limited numerical resolution cannot be blamed for this large discrepancy, since increasing the particle number from 3500 to 58,800 (i.e., increasing spatial resolution by a factor of about 4) results in less than a 20% change in v_{max}(Ni). Furthermore, v_{max}(Ni) does not appear to be a simple monotonically increasing function of the number of particles used. We note that our values for the velocities of each chemical element at 400 minutes after the explosion agree closely with the values published by Arnett et al. (1989b) as well as by Hachisu et al. (1990) and Fryxell et al. (1991) (see Table 1). Thus we conclude that the discrepancy is not related to a particular choice of a numerical method. Finally, we have shown that the exact form of the perturbations introduced in the initial conditions to seed the instabilities has a negligible effect on v_{max}(Ni) ($\lesssim 20\%$), provided that the initial amplitude is big enough ($\gtrsim 5\%$) and the wavelength is greater than the average spacing between the particles.

Having exhausted the list of all potential explanations of the nickel discrepancy within a two-dimensional computational framework, we have performed one simulation in three dimensions. We have modeled a wedge with a 30° opening angle using 100,000 particles. The spatial resolution of this simulation is equivalent to that of an 8000 particle two-dimensional calculation. We find that the velocity distribution of the ejecta is affected very little by this change of geometry. In fact, v_{max}(Ni) changes by less than 20% between our three-dimensional calculation and the two-dimensional computations. We argue that this result will not change significantly with yet another increase in resolution, and conclude that the nickel discrepancy is not an artifact of the two-dimensional geometry used in most published simulations. The three-dimensional simulation reveals a typical "bubbles and spikes" flow pattern with hydrogen in the low-density sinking bubbles and helium and heavier elements in the dense rising spikes. Note that this structure is just the reverse of the usual convective pattern in stars because the relative acceleration is directed outward during the explosion, rather than inward as the pull of gravity usually is.

Facing the fact that no numerical origin of the nickel discrepancy could be found, and that it persists whatever progenitor is used, we conclude that this discrepancy must have its origin in a physical aspect of the problem which has not been accounted for so far. Since we have concentrated our efforts toward eliminating all imaginable late-time ($t > 300$ s) mechanisms as potential culprits, the discrepancy points toward the inadequate modeling of an early-time ($t < 300$ s) phenomenon, which would most likely be the explosion process itself. We conjecture that a first round of instabilities occurs during the explosion which premixes the nickel outward, where it later becomes involved with the shell interface RT instabilities. Thus, the assumption made in simulations that at $t = 300$ s all nickel is still located at the very bottom of the ejecta would appear to be wrong.

To determine the extent of the mixing that would be required from these early instabilities, we artificially premixed nickel in our progenitor to various radii using different distributions and computed the evolution of such models to $t = 90$ days. We found that values of v_{max}(Ni) in good agreement with observations were obtained by uniformly mixing nickel out to about 1.5 $M_\odot$ above the mass cut (through three-quarters of the metal core) in the initial model (see Table 2). We speculate following Colgate (1991) that only convective motions driven by the high-entropy bubble associated with the delayed mechanism can be responsible for such an extent of early nickel mixing. This is investigated in Herant et al. (1991).

We are grateful to E. Müller, K. Nomoto, and S. Woosley for providing us with progenitor models. We would also like to thank F.-K. Thielemann, P. Pinto, R. Kirshner, and M. Davies for suggestions and enlightening discussions. The data shown on Figure 10 were made available to us by the courtesy of J. Spyromilio and M. Haas. This research was supported in part by NASA grant NGR 22-007-272 at Harvard University. One of us (W. B.) also acknowledges partial support from the Swiss National Science Foundation.

APPENDIX A

SYNOPTIC TABLE OF VELOCITIES

There are several reasons why we have chosen to focus our attention on velocity information. First is the fact that, before it starts to interact significantly with the interstellar medium, and after the hydrodynamical instabilities are over, the ejecta has a velocity profile which resembles closely a homologous expansion. It is therefore natural to describe the amount of mixing in velocity space. Further, observations can be most easily related to velocities. Finally, velocities are a quick, straightforward way to compare different simulations with one another. Of course, other features of the problem are important too, such as density contrasts, morphology, etc. However, they are more difficult to quantify, and thus do not lead to a concise overview of the problem, which is the goal of Table 2.

TABLE 2

VELOCITY RESULTS

				400 MINUTES						90 DAYS	
PROGENITOR (1)	COMMENTS (2)	E (3)	NUMBER OF PARTICLES (4)	v_{min}(H) (5)	v_{max}(He) (6)	$\bar{v}$(He) (7)	v_{max}(CO) (8)	$\bar{v}$(CO) (9)	v_{max}(Ni) (10)	v_{min}(H) (11)	v_{max}(Ni) (12)
Nomoto's Progenitor (§§ 2 and 3)											
Nomoto		1.0	3500	700	2600	1850	2550	1550	1000	1050	1550
Nomoto		1.0	8200	700	2650	1950	2550	1500	1100	1050	1750
Nomoto		1.0	23000	550	2650	1950	2600	1500	1100	900	1650
Nomoto		1.0	58800	550	2700	2000	2550	1550	1350	900	1950
Nomoto		2.0	34900	650	3300	2400	3200	1850	1450	1000	1900
Nomoto	±5% perturbations	1.0	23000	900	2400	1900	2300	1450	1000	1200	1800
Nomoto	±1% perturbations	1.0	23000	1800	2150	1750	1850	1400	1050	1750	1750
Nomoto	20 × 40 grid	1.0	23000	750	2650	1950	2450	1500	1000	1000	1700
Other Progenitors (§ 3)											
Woosley		1.5	23700	1050	2250	1550	1050	750	550	1150	1150
Weaver		1.5	26200	†1150	†2550	†1900	†1650	†1150	†1050	1200	1750
Arnett		1.0	25900	†300	†2000	†1300	†1700	†1050	†750	700	1450
Three-dimensional Simulation (§ 4)											
Nomoto	3D	1.0	97500	†300	†2550	†1900	†2450	†1550	†1400	‡600	‡1800
Premixed Progenitors (§ 5)											
Nomoto	Quadratic	1.0	24900	650	2750	2000	2700	1550	2300	750	2350
Nomoto	Exponential	1.0	24900	550	2750	2000	2700	1550	2350	850	2350
Nomoto	Uniform	1.0	24900	550	2750	2000	2700	1550	2350	650	2450
Nomoto	Uniform	2.0	22700	700	3300	2350	3250	1800	3000	800	3050
Results from Other Groups											
Arnett	FAM91	1.0	N/A	200	2050	~1400	1950	~1200	N/A	N/A	N/A
Nomoto	HMNS90	1.0	N/A	800	2300	~2000	2200	~1600	2000	N/A	N/A

NOTE.—Velocities marked with a dagger are for $t = 1000$ minutes, and those marked with a double dagger are for $t = 50$ days.

A1. COLUMNS

Column (1) of the table identifies the presupernova progenitor used in the simulation (cf. § 3). Nomoto's progenitor is described in Shigeyama & Nomoto (1990). Arnett's progenitor is described in Arnett (1987), but one should note that his group has changed progenitors since then. Woosley's progenitor is described in Woosley et al. (1988), and Weaver's progenitor will be described in Weaver & Woosley (1991). Column (3) (E) gives the explosion energy used in the one-dimensional simulation of the progenitor explosion. Column (4) indicates the number of particles (rounded to the nearest hundred) used for the SPH simulation.

Columns (5)–(10) give results at a time 400 minutes after the explosion, before the effect of the radioactive decays starts to be signifant. Columns (11) and (12) give results at a time 90 days after the explosion, after most of the decay energy has been released. All radial velocities are given in kilometers per second rounded to the nearest 50 km s^{-1}. Mean velocities are mass-weighted averages for a given chemical species. CO refers to the "metals," i.e., anything which is heavier than helium but which is not nickel. The velocities of CO and He are almost unchanged by the nickel and cobalt decays; this is why they are not given under the 90 days heading. Some simulations did not give a result which had reached homologous expansion by $t = 400$ minutes, because the hydrogen was still flowing inward. Those are marked with daggers, and the velocities were given for $t = 1000$ minutes.

A2. CATEGORIES OF SIMULATIONS

The first group of simulations corresponds to those using the Nomoto progenitor, with a varying degree of resolution, amplitude of the initial perturbations, and amount of explosion energy. See §§ 2 and 3 for additional details. The second group corresponds to SPH simulations which use other progenitors from Woosley & Weaver and from Arnett. In the latter case, the one-dimensional evolution to $t = 300$ s was done by Arnett's group. The third group has a single entry from our three-dimensional simulation. The fourth group corresponds to simulations with various radial dependences of nickel premixing and various explosion energies. In all cases the furthest point of nickel premixing was at 75% of the mass of the CO shell (see § 5). Finally, the fifth group shows results published by other groups. FAM91 refers to Fryxell et al. (1991), and HMNS90 refers to Hachisu et al. (1990). In some cases, velocities were derived by "eyeballing" the relevant velocity plots and are therefore preceded by the symbol $\sim$. "N/A" means not applicable or not available.

APPENDIX B

TWO-DIMENSIONAL SMOOTH PARTICLE HYDRODYNAMICS

Two-dimensional cylindrical SPH is in essence very similar to standard three-dimensional Cartesian SPH. In this Appendix we focus on specific aspects of two-dimensional SPH. For a complete description of the underlying ideas of SPH, the reader is referred to Benz (1990). As usual, a kernel (the smoothing function W) is used to compute smoothed fields and to take derivatives between interpolation points which move with the fluid. Instead of having coordinates (x_i, y_i, z_i) the points now have coordinates (r_i, z_i), to which we shall associate the vector $\boldsymbol{s}_i$ (this is not the usual $\boldsymbol{r}_i$, since this letter is already in use as a coordinate). Let f be a scalar field defined over the (r, z)-plane. We have for the smoothed field

$$\langle f(\boldsymbol{s})\rangle = \int f(\boldsymbol{s}')W(|\boldsymbol{s}-\boldsymbol{s}'|)d\boldsymbol{s}'$$

$$= \sum_j \frac{f_j W(|\boldsymbol{s}-\boldsymbol{s}_j|)}{\langle n^{2D}(\boldsymbol{s}_j)\rangle}.$$

The integral has been discretized by summing over the points of indices j where f is known. The number density n_j^{2D}, which is used to normalize each term of the summation, corresponds to a surface density. Since $n^{2D}(\boldsymbol{s}) = \sum_k \delta(\boldsymbol{s}-\boldsymbol{s}_k)$, we have $\langle n^{2D}(\boldsymbol{s}_j)\rangle = \sum_k W(|\boldsymbol{s}_k-\boldsymbol{s}_j|)$, where the sum is over the neighbors k of point j. Finally,

$$\langle f(\boldsymbol{s})\rangle = \sum_j \frac{f_j W(|\boldsymbol{s}-\boldsymbol{s}_j|)}{\sum_k W(|\boldsymbol{s}_k-\boldsymbol{s}_j|)}.$$

In particular, for the smoothed surface density ρ_i^{2D} at point i we have

$$\rho_i^{2D} = \sum_j \frac{\rho^{2D}(\boldsymbol{s}_j)W_{ij}}{\sum_k W_{jk}}.$$

If the motion of the points is Lagrangian, it can be checked that the quantity $\rho^{2D}(\boldsymbol{s}_j)/(\sum_k W_{jk})$ is constant because of mass conservation. From now on, we rename the interpolation points "particles," and identify the conserved quantity as the mass m_j of particle j. We can then write

$$n_j^{2D} = \frac{\rho_j^{2D}}{m_j} = \frac{\rho_j^{3D}\times 2\pi r_j}{m_j},$$

so that the smoothed quantity f_i evaluated at particle i is given by

$$f_i = \sum_j f(\boldsymbol{s}_j)\frac{m_j W_{ij}}{\rho_j^{2D}} = \sum_j f(\boldsymbol{s}_j)\frac{m_j W_{ij}}{\rho_j^{3D}\times 2\pi r_j}.$$

The standard trick of SPH in evaluating spatial derivatives is to integrate by parts, thereby transferring the derivative operator from the field to the kernel. The boundary term generally disappears because the kernel vanishes far from the particle. Some care is necessary when computing derivatives in two-dimensional cylindrical coordinates; however, gradients retain the same form as in a Cartesian coordinate system. Thus, one can still write

$$\langle \nabla f(s) \rangle = \int \nabla f(s') W(|s - s'|) ds' = [Wf]_{\text{boundaries}} - \int f(s') \nabla W(|s - s'|) ds'$$

$$= \sum_j \frac{f(s_j) \nabla W(|s - s_j|)}{n_j^{2D}} .$$

There are many different ways one can write the momentum equation within the SPH formalism. The one we have chosen has a similar form to the one given in Benz (1990; see paper for the actual algebraic procedure to obtain the equation):

$$\frac{dv_i}{dt} = -\sum \frac{m_j \nabla W_{ij}}{2\pi r_j} \left[\frac{P_j}{(\rho_j^{3D})^2} + \frac{P_i}{(\rho_i^{3D})^2} + \Pi_{ij} \right],$$

where Π_{ij} is the artificial viscosity contribution and is calculated in a way similar to Benz (1990), with, in the case of our supernova simulations, $\alpha = 1.5$ (linear term) and $\beta = 3.0$ (quadratic term). One can see that the symmetry between i and j, which automatically conserves momentum in Cartesian SPH, is broken in two-dimensional cylindrical SPH because of the r_j term. Generally this is not a problem as long as the action occurs sufficiently far from the z-axis, i.e., $r_j \gg h_j$.

The last equation necessary to solve for the hydrodynamical flow is the energy equation. Empirically, we have found that the best formulation of this equation (i.e., the one which conserved energy best) is the following:

$$\frac{du_i}{dt} = \frac{P_i}{(\rho_i^{3D})^2} \sum_j m_j \left(\frac{v_i}{2\pi r_i} - \frac{v_j}{2\pi r_j} \right) \cdot \nabla W_{ij} + \frac{1}{2} \sum m_j \Pi_{ij} \left(\frac{v_i}{2\pi r_j} - \frac{v_j}{2\pi r_i} \right) \cdot \nabla W_{ij} .$$

The kernel which we use is the standard spline kernel of three-dimensional SPH, but the normalization coefficient changes:

$$W(s, h) = \frac{10}{7\pi h^2} \begin{cases} 1 - \frac{3}{2} v^2 + \frac{3}{4} v^3 , & \text{if } 0 \le v \le 1 , \\ \frac{1}{4} (2 - v)^3 , & \text{if } 1 \le v \le 2 , \\ 0 , & \text{otherwise} , \end{cases}$$

where $v = s/h$. During the simulations, we keep the number of neighbors between 15 and 25, by varying h appropriately. It is this dynamic rescaling capability of SPH which enables us to simulate in one run supernova explosions from $t = 300$ s (typical length scale $= 1\ R_\odot$) to $t = 90$ days (typical length scale $= 10{,}000\ R_\odot$), in a completely hands-off approach.

Special thanks are due to R. Stellingwerf for help in developing our two-dimensional SPH cylindrical geometry code.

REFERENCES

Arnett, W. D. 1987, ApJ, 319, 136
Arnett, W. D., Bahcall, J. N., Kirshner, R. P., & Woosley, S. E. 1989a, ARA&A, 27, 629
Arnett, W. D., Fryxell, B., & Müller, E. 1989b, ApJ, 341, L63
Arnett, W. D., & Fu, A. 1989, ApJ, 340, 396
Aufderheide, M. B., Baron, E. A., & Thielemann, F.-K. 1991, ApJ, 370, 630
Bandiera, R. 1984, A&A, 139, 368
Baron, E. A., & Cooperstein, J. 1990, ApJ, 353, 597
Benz, W. 1990, in Numerical Modeling of Nonlinear Stellar Pulsation: Problems and Prospects, ed. J. R. Buchler (Dordrecht: Kluwer), 269
———. 1991, in Late Stages of Stellar Evolution and Computational Methods in Astrophysical Hydrodynamics, ed. C. de Loore (Berlin: Springer), 259
Benz, W., & Thielemann, F.-K. 1990, ApJ, 348, L17
Chevalier, R. A. 1976, ApJ, 207, 872
Clark, D. H., Murdin, P., Wood, R., Gilmozzi, R., Danziger, J., & Furr, A. W. 1983, MNRAS, 204, 415
Colgate, S. A. 1991, in Supernovae, ed. S. E. Woosley (New York: Springer-Verlag), 352
de Gouveia Dal Pino, E. M., & Opher, R. 1989, MNRAS, 240, 573
Dotani, T., et al. 1987, Nature, 330, 230
Ebisuzaki, T., Shigeyama, T., & Nomoto, K. 1989, ApJ, 344, L65
Fesen, R. A., & Kirshner, R. P. 1982, ApJ, 258, 1
Fryxell, B., Arnett, W. D., & Müller, E. 1991, ApJ, 367, 619
Fu, A., & Arnett, W. D. 1989, ApJ, 340, 414
Gehrels, N., MacCallum, C. J., & Leventhal, M. 1987, ApJ, 320, L19
Haas, M. R., Colgan, S. W. J., Erickson, E. F, Lord, S. D., Burton, M. G., & Hollenbach, D. J. 1990, ApJ, 360, 257
Hachisu, I., Matsuda, T., Nomoto, K., & Shigeyama, T. 1990, ApJ, 358, L57
Herant, M., & Benz, W. 1991, ApJ, 345, L412 (HB91)
Herant, M., Benz, W., & Colgate, S. A. 1991, ApJ, submitted
Höflich, O. 1988, in IAU Colloq. 108, Atmospheric Diagnostics of Stellar Evolution, ed. K. Nomoto (Berlin: Springer), 288
Layzer, D. 1955, ApJ, 122, 1
MacAlpine, G. M., McGaugh, S. S., Mazzarella, J. M., & Uomoto, A. 1989, ApJ, 342, 364
MacAlpine, G. M., & Uomoto, A. 1991, AJ, 102, 218
Matz, S. M., Share, G. H., Leising, M. D., Chupp, E. L., Vestrand, W. T., Purcell, W. R., Strickman, M. S., & Reppin, C. 1988, Nature, 331, 416
Mayle, R. W., & Wilson, J. R. 1991, in Supernovae, ed. S. E. Woosley (New York: Springer-Verlag), 333
McCray, R., Shull, J. M., & Sutherland, P. 1988, ApJ, 317, L73
Mönchmeyer, R. 1989, in Proc. Fifth Workshop on Nuclear Astrophysics, ed. W. Hillbrandt & E. Müller (MPA-P1; Garching: MPI), 92
Mönchmeyer, R., & Müller, E. 1989, in Timing Neutron Stars, ed. H. Ögelman & E. van den Heuvel (Dordrecht: Kluwer), 549
Müller, E., Fryxell, B., & Arnett, W. D. 1990, in Proc. Elba Workshop on Chemical and Dynamical Evolution of Galaxies, ed. F. Federini, J. Franco, & F. Matteucci (Pisa: ETS Editrice), 394
———. 1991, A&A, in press
Pinto, P. A., & Woosley, S. E. 1988a, Nature, 333, 534
———. 1988b, ApJ, 329, 820
Ryu, D., & Vishniac, E. T. 1991, ApJ, 368, 411
Saio, H., Nomoto, K., & Kato, M. 1988, Nature, 334, 508
Shigeyama, T., & Nomoto, K. 1990, ApJ, 360, 242

Shigeyama, T., Nomoto, K., & Hashimoto, M. 1988, A&A, 196, 141
Spyromilio, J., Meikle, W. P. S., & Allen, D. A. 1990, MNRAS, 242, 669
Sunyaev, R., et al. 1987, Nature, 330, 227
Tryggvason, G., & Unverdi, S. O. 1990, Phys. Fluids A, 2, 657
Tueller, J., Barthelemy, S., Gehrels, N., Teegarden, B. J., Leventhal, M., & MacCallum, C. J. 1990, ApJ, 351, L41
Weaver, T. A., & Woosley, S. E. 1991, in preparation
Woosley, S. E. 1988, ApJ, 330, 218
Woosley, S. E., Pinto, P., & Weaver, T. A. 1988, Proc. Astron. Soc. Australia, 7, 355
Xu, Y., Sutherland, P., McCray, R., & Ross, R. 1988, ApJ, 327, 197